

An investigation of the thermal stability of $\text{Nd}_x\text{Y}_y\text{Zr}_{1-x-y}\text{O}_{2-6}$ inert matrix fuel materials

John R. Hayes, Andrew P. Grosvenor*

Department of Chemistry, University of Saskatchewan, Saskatoon, SK, S7N 5C9

Mouna Saoudi

Canadian Nuclear Laboratories Limited**, Chalk River, ON, K0J 1J0

*Author to whom correspondence should be addressed

E-mail: andrew.grosvenor@usask.ca

Phone: (306) 966-4660

Fax: (306) 966-4730

**Formerly, Atomic Energy of Canada Limited (AECL)

Abstract

An important step in achieving a closed uranium fuel cycle is to develop new inert matrix fuel (IMF) materials for use in the burn-up of transuranic species (TRU; i.e., Pu, Np, Am, Cm). Cubic fluorite zirconia (ZrO_2) has ideal properties for use in IMF applications, but it is not stable at room temperature and must be stabilized through the addition of small amounts of dopants such as Y. While Y-substituted zirconia (YSZ) has been extensively studied, relatively little work has been done to investigate how the addition of an actinide to the YSZ system affects the properties of these materials. To this end, the long-range and local structures of a series of $\text{Nd}_x\text{Y}_y\text{Zr}_{1-x-y}\text{O}_{2-\delta}$ compounds (Nd was used as a surrogate for Am) were studied using powder X-ray diffraction (XRD), scanning electron microscopy (SEM), and X-ray absorption spectroscopy (XAS) at the Zr K-, Zr L_3 -, Y K-, and Nd L_3 -edges. The thermal stability of Nd-YSZ materials was also investigated by annealing the materials at temperatures ranging between 600-1400 °C. These studies showed that the thermal stability of the $\text{Nd}_x\text{Y}_y\text{Zr}_{1-x-y}\text{O}_{2-\delta}$ system was improved by the addition of small amounts of Y (i.e. ≥ 5 at.%) to the system. Additionally, the XAS results showed that the local structure around Zr remained relatively constant; only changes in the second coordination shell were observed when the materials were annealed. These results strongly suggest that the addition of Y can significantly improve the thermal stability of zirconia-based IMFs. This study has also confirmed the importance and value of using advanced characterization techniques that are sensitive to the local structures of a material (i.e., XAS).

General Keywords: X-ray absorption spectroscopy, nuclear fuel, yttria-stabilized zirconia, structural characterization, inert matrix, fuel cycle

Journal Keywords: EXAFS; nuclear reactor materials; oxide materials; crystal structure; order-disorder effects; phase transitions

1. Introduction

The use of inert matrix fuels (IMF) has been proposed to “burn-up” (transmute) transuranic elements (TRU; i.e., Pu, Np, Am, Cm) using currently available commercial pressurized-water reactors (PWR) [1–3] to reduce the heat load generated by these TRU species in nuclear waste [4]. IMFs consist of actinides embedded in a neutron transparent (inert) matrix, and, unlike the mixed-oxide (MOX) (Pu,U)O₂ fuels currently used, allow TRU burn-up without breeding Pu in the process [5]. The higher burn-up efficiency of IMF materials means that a smaller IMF loading is required in the reactor core, and makes IMFs economically comparable to MOX fuels [5]. In addition, IMFs may be designed to act as a geological storage matrix, eliminating the need for expensive post-service reprocessing [1–3,5–7].

In order for a material to be considered for use in IMF applications, the material should exhibit: favorable neutronic properties, compatibility with the reactor coolant, ability to withstand high radiation doses, high thermal conductivity, and the ability to incorporate burnable poisons such as Gd and Er [5]. Cubic zirconia (ZrO₂), adopting the fluorite-type structure (Figure 1), is a material that has been shown to retain its mechanical and chemical stability under extreme temperature and irradiation conditions. As such, this material has been studied extensively for use in IMF applications [3,8–18]. However, pure cubic zirconia is only stable at temperatures above 2370 °C, and adopts a tetragonal structure at temperatures between 1170 °C–2370 °C and a monoclinic structure at temperatures below 1170 °C [19,20]. These structures are highly related, and the tetragonal and monoclinic structures may be considered as distortions of the parent cubic structure [21]. It is well known that the cubic structure can be stabilized by doping the material with aliovalent cations such as Ca²⁺ or Y³⁺. The size difference between Zr and the doped cation in addition to O-vacancies generated due to charge-balancing requirements act to stabilize the cubic structure across a range of temperatures [22,23]. Yttria-stabilized zirconia (YSZ) has been extensively studied for use in IMF applications, likely due to the extensive knowledge base generated on YSZ from its use and study as a structural ceramic in the nuclear industry [24,25]. Additionally, YSZ has been widely studied as a solid-oxide fuel cell material and a thermal barrier coating [26–28]. However, relatively little research has been performed to understand how the addition of an actinide element to the YSZ system will affect the thermal stability of these materials.

The extremely complex reactions and changes in composition that occur within a nuclear fuel during service make it necessary to understand how the structure of actinide-doped YSZ materials will change when they are subjected to a wide range of temperatures over a range of actinide doping levels. A phase change from a cubic structure to a lower symmetry structure will result in a decrease in the thermal conductivity of the fuel material, which could lead to an unsafe increase in the reactor core temperature [29–31]. Further, the phase transition from the cubic to monoclinic structure is accompanied by a 3-5% increase in volume [20,32]. Given the extremely precise manufacturing tolerances of a fuel rod, this expansion could lead to fuel cladding failures, allowing fission products to be released into the reactor coolant system. Additionally, it has been previously shown that the properties of tetragonal ZrO_2 such as its mechanical stability deteriorate drastically when exposed to water at 300 °C - 400 °C [20]. Given the possible consequences of fuel failure and the need to control and reduce the risks associated with nuclear power, it is necessary to thoroughly characterize these materials to obtain an understanding of the fundamental properties of any potential IMF material before it can be used in commercial service.

To this end, the thermal stability of a series of Nd-doped YSZ materials ($Nd_xY_yZr_{1-x-y}O_{2-\delta}$; $0 \leq x \leq 0.30$, $0 \leq y \leq 0.30$) has been studied. (Due to the similarity of their ionic radii and oxidation state, Nd^{3+} was used as a surrogate for Am^{3+} [33–36].) The materials were annealed at multiple temperatures ranging from 600 °C – 1400 °C and characterized using powder X-ray diffraction (XRD), scanning electron microscopy (SEM), and X-ray absorption spectroscopy (XAS). While powder XRD allowed for characterization of the long-range structure with annealing, XAS allowed for characterization of the local structures around the individual metal centres at a scale not easily observable by XRD. This study has proved that the structure of cubic $Nd_xY_yZr_{1-x-y}O_{2-\delta}$ materials is stable across a wide range of temperatures and compositions when $y \geq 0.05$.

2. Experimental

2.1. Synthesis

The $Nd_xY_yZr_{1-x-y}O_{2-\delta}$ ($0 \leq x \leq 0.30$, $0 \leq y \leq 0.30$) compounds were synthesized via a standard solid-state synthesis. Briefly, stoichiometric amounts of Nd_2O_3 (Alfa Aesar, 99.9%), Y_2O_3 (Alfa Aesar, 99.99%), and ZrO_2 (Alfa Aesar, 99.978%) powders were ground and mixed together under acetone using an agate mortar and pestle. The mixture was then pressed into a pellet at 8 MPa and heated in an alumina crucible at 1500 °C for six days

with intermittent grinding and quenched in air. The thermal stability of the $\text{Nd}_x\text{Y}_y\text{Zr}_{1-x-y}\text{O}_{2-\delta}$ compounds was studied by annealing the as-synthesized materials at 600 °C, 900 °C, 1200 °C, and 1400 °C. The annealed samples studied by XAS and powder XRD were prepared by annealing ~0.07 g aliquots of the as-synthesized material for five days as free powders.

The phase analysis of the materials was performed using powder X-ray diffraction. The powder X-ray diffraction patterns were collected using a PANalytical Empyrean diffractometer set-up in a Bragg-Brentano geometry using either Cu $K_{\alpha 1,2}$ ($\lambda=1.5406 \text{ \AA}$) or Co $K_{\alpha 1,2}$ ($\lambda=1.7890 \text{ \AA}$) radiation. Patterns were collected from 10-90° 2 θ using a 0.017° step-size and a dwell time of 31.1 s/step. The unit cell parameters and the weight amounts of the crystallized phases of the synthesized materials were quantified by Rietveld refinement using the PANalytical HighScore Plus software [37]. Rietveld refinements were performed by fitting cubic ZrO_2 , tetragonal ZrO_2 , and monoclinic ZrO_2 phases to the data [38–40]. The phases used to model the diffraction data were adapted from the pure ZrO_2 patterns by artificially adding Nd and Y to the crystallographic site occupied by Zr. The site occupancies were set to be consistent with the ideal stoichiometry of each material. As an example, the cubic ZrO_2 pattern for the $\text{Nd}_{0.10}\text{Y}_{0.10}\text{Zr}_{0.80}\text{O}_{1.90}$ pattern was generated by adding Y and Nd to the Zr 4a site. The Zr site occupancy was set to 0.80 while the Y and Nd site occupancies were each set to 0.10. The addition of Y and Nd impacted the intensity of the modelled peaks and significantly improved the quality of the fit. The background was fitted using a 3rd order polynomial function which also included a 1/2 θ term [37].

2.2. Scanning Electron Microscopy

SEM samples were prepared by pressing ~0.17 g of the as-synthesized material into a 1/4" (0.635 cm) pellet at 8 MPa, and then then sintering the pellets at 1500 °C for 12 h. The pellets for SEM analysis were annealed at the given temperature for five days and air quenched. Several of the pellets were cut using a diamond saw and mounted to allow for imaging of the pellet cross-section. The pellets were embedded in a resin matrix and ground manually to a flat surface using SiC paper. The pellet surfaces were then polished using 0.25 μm diamond paste. The samples were coated with a thin carbon layer to reduce sample charging effects. A Zeiss Supra-55 WDS-VP SEM coupled with an Energy Dispersive X-ray Spectrometer (EDS) was used to collect SEM images and to carry out EDS mapping. Secondary electron (SE) images were collected to study the surface topography and backscatter electron (BSE) images were collected to study the Nd-distribution in the zirconia

matrix. Samples were mapped by EDS for Zr and Nd at 500x magnification, and the EDS maps were collected using an ~ 8 μm step size at an accelerating voltage of 20 kV.

2.3. X-ray Absorption Spectroscopy Measurements

2.3.1. Zr K-, Nd L₃-, and Y K-edge XAS

Zr K-, Nd L₃-, and Y K-edge XAS spectra from the as-synthesized and annealed samples were collected using the Pacific Northwest Consortium/X-ray Sciences Division Collaborative Access Team (PNC/XSD-CAT, Sector 20) bending magnet beamline (20BM) located at the Advanced Photon Source (APS) at Argonne National Laboratory. A silicon (111) double crystal monochromator with a Rh harmonic rejection mirror was used, which has a resolution of 2.4 eV and a photon flux of $\sim 10^{11}$ photons/s at 17 keV [41]. The samples were finely ground and sealed between layers of Kapton tape and the number of layers was adjusted to maximize the absorption signal. Samples were mounted at an angle of $\sim 45^\circ$ to the incident beam.

The Zr K-edge and Y K-edge XAS spectra were collected in transmission mode. The incident beam intensity (I_0) was measured with a N₂-filled ion chamber and the transmission spectra were measured with ion chambers filled with an 80% N₂-20% Ar gas mixture. Both the Zr K- and Y K-edge spectra were calibrated using Zr metal foil, having a known Zr K-edge absorption energy of 17998 eV [42]. The Zr metal foil spectrum was measured concurrently with the Zr K-edge spectra from the samples. During collection of the Y K-edge spectra, Zr metal foil XAS spectra were measured separately for calibration. The X-ray absorption near-edge (XANES) region of the Zr K- and Y K-edge spectra were measured using a 0.3 eV step through the edge. The extended x-ray absorption fine structure (EXAFS) region of the Zr K-edge spectra was measured to $k = 15$ and the EXAFS of the Y K-edge was measured to $k = 14$.

The Nd L₃-edge spectra were collected in transmission mode and the incident beam intensity was measured with an ion chamber filled with an 80% He-20% N₂ gas mixture. The transmission spectra were collected using N₂-filled ion chambers. The spectra were calibrated using a Mn foil, which was measured separately and has a known absorption-edge energy of 6539 eV [42]. The Nd L₃-edge XANES region was measured using a 0.15 eV step through the edge and measured to $k = 10.5$. (The Nd L₃-edge is limited by the presence of the Nd L₂-edge at 6722 eV.) All XAS spectra discussed in this article were normalized and analyzed using the Demeter software suite (i.e., Artemis and Athena) [43].

2.3.1.1. Analysis of Zr K- and Y K-edge EXAFS Spectra

The EXAFS spectra were analyzed by fitting the parameters of the standard EXAFS equation:

$$\chi(k) = \sum_j \frac{N_j S_o^2}{k R_j^2} F_j(k) e^{-2\sigma_j^2 k^2} e^{-2R_j/\lambda} \sin(2kR_j + \phi_j(k))$$

where N_j is number of j^{th} atoms at a distance R_j from the absorbing atomic centre, $F_j(k)$ is the backscattering function, σ_j^2 is the Debye-Waller Factor, and $\phi_j(k)$ is the phase-shift function of the j^{th} atom. $F_j(k)$ describes how strongly the photoelectron scatters off the neighboring atom and $\phi_j(k)$ describes how the phase of the photoelectron shifts upon scattering. Both functions are dependent on the neighbouring atom atomic number (Z), which makes the EXAFS phenomenon chemically sensitive [44]. S_o^2 is the amplitude factor and λ is the inelastic mean-free path of the photoelectron [44]. N_j is equivalent to the coordination number for single-scattering paths, and will be referred to here as CN (i.e., coordination number). The EXAFS spectra were analyzed by calculating $F_j(k)$, $\phi_j(k)$ and λ for each set of scattering pairs in a given cluster using the FEFF6 code [45]. The other parameters were fit using a least-squares refinement as described below using the program Artemis, which is included in the Demeter software suite [43].

A scattering cluster was generated using the cubic zirconium structure with lattice constants determined from the powder XRD patterns (*vide infra*). An appropriate amount of Zr in the second coordination shell was replaced by Nd before conducting the FEFF calculation. Multiple calculations with Nd located at different sites were performed, and it was determined that the results of the FEFF calculations were independent of the locations of the Nd substitutions. Zr and Y were treated as equivalent atoms in this model, as the atomic numbers of Y and Zr (39 and 40, respectively) were similar and no significant changes in the scattering amplitude and phase shift functions were observed [46]. The model was constructed using four single scattering paths. The single scattering paths were the nearest neighbor Zr–O path, the next-nearest neighbor Zr–Zr/Y and Zr–Nd paths, and the third shell Zr–O scattering path (labelled here as Zr–O2). The CN of each scattering path was set manually. The amplitude factor, S_o^2 , and energy shift, ΔE_o , were fitted across all scattering paths. The changes in the scattering path lengths, ΔR , and the Debye-Waller factor, σ^2 , of each single-scattering path were individually fitted. In addition to the single-scattering paths, two multi-scattering paths corresponding to the three-legged Zr–O–Zr/Y

and Zr–O–Nd scattering paths were also fitted. The changes in multi-scattering path lengths were modelled as $2\Delta R_{\text{Zr-O}} + \Delta R_{\text{Zr-Zr/Y/Nd}}$, and the Debye-Waller factors were modelled as $2\sigma^2_{\text{Zr-O}} + \sigma^2_{\text{Zr-Zr/Y/Nd}}$.

The central Zr atom in the scattering cluster was replaced by Y in the model used to fit the Y K-edge spectra. The Y K-edge EXAFS spectra were fitted using a model similar to the one used to fit the Zr K-edge spectra. The Y K-edge spectra were fitted using Y–O, Y–Zr/Y, Y–Nd single scattering paths, and the third shell Y–O single scattering paths (labelled as Y–O2). The Y–O–Y/Zr and Y–O–Nd multi-scattering paths were also included in the fit. The CN was set manually in all cases. The restraints used for the multi-scattering paths were analogous to those used to fit the Zr K-edge.

2.3.2. Zr L₃-edge XANES

Zr L₃-edge XANES spectra were collected using the Soft X-ray Microcharacterization Beamline (SXRMB, 06B1-01) located at the Canadian Light Source (CLS). The beamline has a photon flux of $>1 \times 10^{11}$ photons/s and provides a resolution of ~ 0.25 eV when using a Si (111) crystal monochromator at X-ray energies less than 2500 eV [47]. Samples were prepared by applying the finely ground powder to Kapton tape and adhering the Kapton tape onto the sample holder using double-sided C tape. Spectra were measured in total electron yield (TEY) mode using a 0.10 eV step through the absorption edge. Spectra were calibrated using Zr foil, which has a known Zr L₃-edge absorption energy of 2223 eV [42].

3. Results

3.1. Powder X-ray Diffraction

Powder XRD patterns from the as-synthesized and annealed compounds are presented in Figure 2, and Figures S1 and S2 in the Supporting Information (SI). The unit-cell parameters and phase quantification of these materials was determined by Rietveld refinement, and the results of this analysis are summarized in Table 1 and Table S1 in the SI. The size of the unit cell decreased linearly as the Y content increased at constant Zr concentrations in $\text{Nd}_x\text{Y}_y\text{Zr}_{1-x-y}\text{O}_{2-\delta}$, consistent with Vegard's Law. [48]. No significant changes in the unit cell parameters were observed when any of the materials synthesized at 1500 °C were subsequently annealed at temperatures up to 1400 °C.

The calculated pattern obtained by Rietveld refinement consistently underfitted the intensities of the (311) and (222) peaks found at $\sim 69.6^\circ$ and $\sim 73.2^\circ$, respectively. Changes from the ideal site occupancies based on the ideal stoichiometry of each material could affect the intensities of these reflections, accounting for the mismatch in peak intensities. Additionally, a slight preferential orientation away from the (100) direction was observed in several compounds. (The preferred orientation factor varied from 0.93 to 1.02.)

In general, all of the ternary $\text{Nd}_x\text{Zr}_{1-x}\text{O}_{2-\delta}$ materials studied that were synthesized at 1500 °C were stable up to and including a post-annealing temperature of 900 °C. However, two peaks at $\sim 32.8^\circ$ and 36.7° associated with monoclinic ZrO_2 and one at $\sim 34.3^\circ$ associated with tetragonal ZrO_2 were observed when $\text{Nd}_{0.25}\text{Zr}_{0.75}\text{O}_{1.88}$ was annealed at 1400 °C (Figure 3). The concentrations of each phase in this system were determined to be 11.3% the monoclinic phase, 4.2% the tetragonal phase, and 84.5% the cubic phase (see Table 1). This result indicated that the cubic structure of the ternary Nd-stabilized zirconia sample was not stable when annealed at this temperature. No peaks associated with lower-symmetry zirconia phases were observed when the quaternary Nd-YSZ materials were annealed at 1400 °C (cf. Figure 2b, Figures S1 and S2). The powder XRD results showed that the long-range cubic fluorite structure can be stabilized by the addition of a small amount of Y^{3+} to the $\text{Nd}_x\text{Zr}_{1-x}\text{O}_{2-\delta}$ system.

3.2. SEM and EDS

SEM micrographs were collected from several of the pellets and these are presented in Figure 4 and Figures S3-S7. The micrographs were collected in secondary electron (SE; Figure 4a,c) and backscattering electron (BSE; Figure 4b,d) modes, which allowed for an examination of both the surface topography and the distribution of Nd in the sample. No significant changes in the porosity or topography of any of the pellet surfaces were observed when the $\text{Nd}_x\text{Y}_y\text{Zr}_{1-x-y}\text{O}_{2-\delta}$ materials were annealed at 1400 °C (Figure 4a,c, Figures S3-S7). This observation indicates that the pellets did not crack or degrade during the annealing process.

Several bright spots were observed in the BSE images from both the as-synthesized and annealed $\text{Nd}_x\text{Y}_y\text{Zr}_{1-x-y}\text{O}_{2-\delta}$ materials (Figures 4b,d, Figures S3-S7). The bright spots are indicative of regions of high Nd concentration because Nd scatters electrons much more efficiently than Zr or Y due to the higher atomic number of Nd. The heterogeneous distribution of Nd within the materials was confirmed by the Nd L_α EDS maps, as shown in Figure 5 and Figures S3-S7. The EDS maps show that no significant change in the Nd distribution occurred upon annealing.

The Zr L_{α} EDS maps presented in Figure 6 showed that there was a significant segregation of Zr in the ternary $\text{Nd}_x\text{Zr}_{1-x}\text{O}_{2-\delta}$ materials, and the number of Zr inclusions increased when the materials were annealed at 1400 °C. The presence of Zr inclusions in $\text{Nd}_x\text{Zr}_{1-x}\text{O}_{2-\delta}$ could be indicative of the formation of small islands of monoclinic ZrO_2 , which is consistent with the powder XRD results that showed monoclinic and tetragonal ZrO_2 phases were formed when $\text{Nd}_{0.25}\text{Zr}_{0.75}\text{O}_{1.88}$ was annealed at 1400 °C (*vide supra*). In contrast, no obvious Zr inclusions were observed in the Zr EDS maps from any of the quaternary $\text{Nd}_x\text{Y}_y\text{Zr}_{1-x-y}\text{O}_{2-\delta}$ materials. These results indicate that the addition of a small amount of Y will increase the thermal stability of $\text{Nd}_x\text{Zr}_{1-x-y}\text{O}_{2-\delta}$ materials.

3.3. Zr K-edge XAS

3.3.1. XANES

The Zr K-edge XANES spectra collected from the as-synthesized and annealed $\text{Nd}_x\text{Y}_y\text{Zr}_{1-x-y}\text{O}_{2-\delta}$ compounds are presented in Figure 7 and Figure S8 in the SI. Three features were observed in these spectra, which are labelled as A, B, and B' in Figure 7a. Feature A is attributed to dipole-forbidden (quadrupolar) $\text{Zr } 1s \rightarrow \text{Zr } 3d$ transitions, and features B and B' are attributed to the dipole-allowed $\text{Zr } 1s \rightarrow \text{Zr } 4p$ transitions [49,50]. The Zr K-edge spectra did not change when the composition was changed (Figure 7a). However, a small increase in the intensity of the feature located at ~18020 eV was observed when $\text{Nd}_{0.25}\text{Zr}_{0.75}\text{O}_{2-\delta}$ was annealed at 1400 °C (Figure 7b). This change can be understood by comparing these spectra to the spectra collected from tetragonal ZrO_2 ($\text{Y}_{0.09}\text{Zr}_{0.91}\text{O}_{1.96}$) and monoclinic ZrO_2 (Figure 7c). The energy difference between features B and B' decreases as the symmetry of the structure decreases, resulting in an increase in the intensity at ~18020 eV. Based on this comparison to the spectra from the Zr standards, the change in the spectra from $\text{Nd}_{0.25}\text{Zr}_{0.75}\text{O}_{1.88}$ upon annealing is attributed to the formation of tetragonal and/or monoclinic ZrO_2 . This result is consistent with the powder XRD results which showed that monoclinic and tetragonal ZrO_2 was formed when the $\text{Nd}_{0.25}\text{Zr}_{0.75}\text{O}_{1.88}$ material was annealed at 1400 °C (*vide supra*). No changes were observed when the other $\text{Nd}_x\text{Y}_y\text{Zr}_{1-x-y}\text{O}_{2-\delta}$ materials were annealed at temperatures up to 1400 °C (cf. Figure 7b, Figure S8), which is also consistent with the powder XRD results. These results show that the addition of Y^{3+} stabilized the cubic structure of $\text{Nd}_x\text{Y}_y\text{Zr}_{1-x-y}\text{O}_{2-\delta}$.

3.3.2. EXAFS

The Zr K-edge EXAFS spectra were collected from the as-synthesized and annealed $\text{Nd}_x\text{Y}_y\text{Zr}_{1-x-y}\text{O}_{2-\delta}$ materials to better understand how the local structure around Zr changed with composition and annealing temperature. The Fourier transformed EXAFS spectra from the as-synthesized samples are presented in Figure 8a. These spectra have two prominent peaks, which are labelled as C and D. Peak C is attributed to scattering in the first shell between Zr and the nearest-neighbour O atoms, and peak D is attributed to the second shell scattering path between Zr and the next-nearest-neighbour (NNN) Zr, Y, and Nd atoms. The intensity of Peak C did not change with Nd content while the intensity of peak D decreased with increasing Nd content.

It has been previously suggested that the decrease in the intensity of feature D is due to an increase in the disorder of the second shell cations [51]. However, an examination of the real portion of the Fourier transformed EXAFS spectra, shown in Figure 8b, indicates that this decrease may in fact be due to changes in the backscattering amplitude function ($F_j(k)$) and phase-shift function ($\phi_j(k)$) of the NNN atoms. It can clearly be seen from the plots in Figure 8b and 8c that the amplitude of the Zr–Zr/Y/Nd scattering path decreases with increasing Nd content, and that the decrease in feature D is due to changes in the phase-shift function ($\phi_j(k)$) and backscattering amplitude function ($F_j(k)$) between the Zr–Nd and Zr–Zr/Y scattering paths. (The Zr–Zr and Zr–Y scattering paths were treated as being identical during this analysis given the similar atomic numbers of Zr and Y.) Therefore, the change in the intensity of peak D is attributed to the differences between the Zr–Zr and Zr–Nd phase-shift and amplitude functions, and is not due to structural changes.

The changes observed in the EXAFS spectra from $\text{Nd}_{0.25}\text{Zr}_{0.75}\text{O}_{1.88}$ when it was annealed at different temperatures are presented in Figure 9a. Only minimal changes in the intensity of feature C were observed; however, the intensity and peak width of feature D decreased when the material was annealed at 1400 °C. This change likely occurred due to increased disordering in the second shell (*vide infra*). In contrast, only small changes in feature C and almost no changes in feature D were observed when the quaternary $\text{Nd}_x\text{Y}_y\text{Zr}_{1-x-y}\text{O}_{2-\delta}$ materials were annealed (Figure S9).

The results of the fits of the EXAFS data are presented in Table 2 and Table S2, and are plotted in Figure 9 and Figures S10-S16. The Zr–O bond length was determined to be 2.16 ± 0.01 Å in all the materials studied, which is in good agreement with previously reported results from cubic zirconia materials [16,46,52,53]. The Zr–O bond length and Debye Waller factor (σ^2) were independent of composition and annealing temperature,

indicating that the local Zr–O coordination environment remained unchanged upon annealing. The Zr–Zr/Y bond lengths were determined to be 3.55 ± 0.01 Å, which is again in good agreement with previously reported results [46,52]. The Zr–Nd bond length was found to vary between 3.7–3.8 Å. The Zr–Zr and Zr–Nd bond lengths are only slightly less than the bond length predicted using the ionic radii of Zr^{4+} and Nd^{3+} [34]. The Zr–O₂ bond distance was found to be 4.34–4.43 Å, though the error for this value was found to be large (± 0.07 Å). In general, the Zr–O₂ scattering path did not contribute significantly to the fitted model of the EXAFS spectra.

The Debye-Waller factor of the Zr–Zr/Y scattering paths did not vary significantly with changes in composition or annealing temperature in all the materials studied. However, the Debye-Waller factor of the Zr–Nd path nearly doubled when the $Nd_{0.25}Zr_{0.75}O_{1.88}$ material was annealed at 1400 °C. The Debye-Waller factor contains contributions from both static disorder and thermal disorder, and an increased value indicates more disorder in the system [44]. The thermal disorder is expected to remain nearly constant as all spectra were collected at room temperature [54]. Therefore, the observed changes in the Debye-Waller factor are likely attributable to changes in the static disorder of the system. The EXAFS results indicate that while the local coordination environment around Zr remains relatively constant, the extended system becomes disordered when $Nd_{0.25}Zr_{0.75}O_{1.88}$ is heated at 1400 °C. The Zr K-edge EXAFS results also show that this disordering does not occur in the quaternary $Nd_xY_yZr_{1-x-y}O_{2-\delta}$ materials (see Table 2 and Table S2).

3.4. Zr L₃-edge XANES

Zr L₃-edge XANES spectra collected from several of the as-synthesized and annealed $Nd_xY_yZr_{1-x-y}O_{2-\delta}$ compounds, as well as monoclinic ZrO₂ are presented in Figure 10. The Zr L₃-edge is attributable to Zr 2p → Zr 4d transitions, and the two observed features (E and F in Figure 10) are due to the crystal field splitting of the Zr 4d states. Feature E is attributed to Zr 2p → Zr 4d e_g transitions while feature F is attributed to Zr 2p → Zr 4d t_{2g}* transitions [55,56].

The features in the spectra from the $Nd_xY_yZr_{1-x-y}O_{2-\delta}$ materials were more intense and sharper than the features observed in the spectrum from monoclinic ZrO₂. Additionally, a feature observed at ~2225 eV in the monoclinic ZrO₂ spectrum is not present in the spectra from $Nd_xY_yZr_{1-x-y}O_{2-\delta}$. The intensity of Feature F was observed to increase as the amount of Nd in the $Nd_xY_yZr_{1-x-y}O_{2-\delta}$ materials decreased. The origin of these changes may be caused by a shift to a more symmetric coordination environment around the Zr centres. This increase in

symmetry results in more degenerate 3d states, leading to narrower, more intense peaks [55]. These results indicate that the symmetry of the Zr coordination environment increased as Y replaced Nd in the $\text{Nd}_x\text{Y}_y\text{Zr}_{1-x-y}\text{O}_{2-\delta}$ system. The Zr L_3 -edge is more sensitive to changes in the geometry of the Zr coordination environment than the Zr K-edge, which is why the Zr K-edge XANES and EXAFS spectra did not indicate there were changes in the local coordination environment. These results indicate that changes in the coordination geometry of Zr occurred when Y replaced Nd in the quaternary $\text{Nd}_x\text{Y}_y\text{Zr}_{1-x-y}\text{O}_{2-\delta}$ system.

3.5. Y K-edge EXAFS

The EXAFS region of the Y K-edge spectra allows for an understanding of how the local structure around Y in the $\text{Nd}_x\text{Y}_y\text{Zr}_{1-x-y}\text{O}_{2-\delta}$ materials changed with both composition and annealing temperature. The Fourier transformed EXAFS spectra from several of the as-synthesized materials are presented in Figure 11. These spectra strongly resembled the Zr K-edge EXAFS spectra, and exhibited two main peaks, labelled as G and H. Similar to the Zr K-edge, peak G is attributed to first shell Y–O scattering paths and feature H is attributed to scattering between Y and the second-shell cation ions (i.e., Y, Zr, and Nd). The intensity of peak H decreased as the Nd content increased, and the intensity of peak G did not change with changing Nd content. The change in the intensity of peak H can be attributed to the difference in the scattering amplitude and phase shift functions of Nd compared to Y, similar to the Zr K-edge EXAFS spectra discussed in section 3.3.2. The Fourier transform of the Y K-edge EXAFS spectra from the as-synthesized and annealed materials are compared in Figure 12a and Figure S17. These comparisons show that no significant changes in the EXAFS spectra are observed when the materials were annealed. Therefore, it can be concluded that the Y coordination environment did not change with annealing temperature.

The EXAFS spectra were fitted using models similar to the ones constructed to analyze the Zr K-edge EXAFS spectra, and are plotted in Figure 12 and Figure S18. The parameters determined from this fit are given in Table 3 and Table S3 in the SI. The first shell Y–O bond distance was determined to be 2.33 Å, consistent with previous literature reports [15,46,51,52]. This value is smaller than expected from the sum of the Y^{3+} and O^{2-} ionic radii when Y is in an eight-fold coordination environment, and, instead, this bond distance is more consistent with Y occupying a 7-fold coordination environment [15,34,46]. It has been previously suggested that the reduced Y–O bond distance is caused by compression of the Y–O polyhedra, and is not indicative of a reduced coordination

number [15,46]. The Debye-Waller factor (σ^2) was only slightly elevated (0.009 \AA^2) when the CN was set to 8. However, σ^2 and CN are correlated, and an overly large CN would result in a large σ^2 value. Therefore, it is concluded here that the Y CN was 8. In all cases, the Y–O bond distance and σ^2 were independent of composition and annealing temperature, indicating that the Y-coordination environment was not sensitive to these variables.

The second shell Y–Zr/Y bond distance was determined to be $3.63 \pm 0.01 \text{ \AA}$, and the bond length was independent of both composition and annealing temperature. This value is within error of the 3.64 \AA metal–metal bond distance determined from XRD and is only slightly contracted from the value calculated using the Zr–O and Y–O bond lengths determined from the EXAFS fits. In contrast, the Y–Nd bond distance in $\text{Nd}_{0.20}\text{Y}_{0.05}\text{Zr}_{0.75}\text{O}_{2-\delta}$ determined from the fit of the EXAFS data was found to be between $3.4\text{--}3.5 \text{ \AA}$, which is significantly less than the expected value of 3.94 \AA based on the Y^{3+} and Nd^{3+} ionic radii. The Debye-Waller factor (σ^2) of the Y–Nd shell was determined to be $0.02\text{--}0.03 \text{ \AA}^2$, which is unreasonably large. The large σ^2 value shows that there is significant disorder in the second shell Y–Nd scattering paths. The large σ^2 value could also indicate that too large a CN was used, given that the CN and σ^2 are highly correlated. This likely indicates that Nd and Y were not homogeneously distributed, and that Nd preferentially occupied sites that were not adjacent to Y atoms.

The fitted Y–Nd bond distance is unreasonable within the fluorite structure, and likely represents a failure in the fitting model. However, a 3.4 \AA Nd–Y bond distance is found in the structure of B-phase mixed RE_2O_3 sesquioxides (RE = Rare-earth, Y, Sc), and the fitted result could possibly indicate that such a phase is present here [57]. Calculated $\text{Y}_2\text{O}_3\text{--Nd}_2\text{O}_3$ phase diagrams also support the possible presence of a B-phase $\text{Nd}_{2-x}\text{Y}_x\text{O}_3$ type material as the B-phase is stabilized at Y_2O_3 mole fractions as low as 0.16 [58]. The presence of such a phase is also supported by a previous study of Y-doped CeO_2 by XRD [57]. If a B-phase $\text{Nd}_{2-x}\text{Y}_x\text{O}_3$ was formed in the materials studied here, it is likely that it would not be observable by conventional powder XRD given the low concentration and low symmetry of this phase, and further investigation is necessary to confirm if B-phase $\text{Nd}_{2-x}\text{Y}_x\text{O}_3$ is present in this system.

3.6. Nd L_3 -edge XANES

The Nd L_3 -edge XANES spectra were collected from several of the $\text{Y}_y\text{Nd}_x\text{Zr}_{1-x-y}\text{O}_{2-\delta}$ materials and these spectra are presented in Figure 13. A single, intense feature is observed in these spectra, which corresponds to excitation of the Nd 2p electrons to Nd 5d valence states [59]. There were no changes in the Nd L_3 -edge XANES

spectra when any of the as-synthesized $\text{Nd}_x\text{Y}_y\text{Zr}_{1-x-y}\text{O}_{2-\delta}$ materials were annealed (Figure 13b). This likely indicates that the local coordination environment around Nd was stable for all of the materials studied.

4. Discussion

The results presented above show that the $\text{Nd}_x\text{Zr}_{1-x}\text{O}_{2-\delta}$ materials synthesized at 1500 °C undergoes a partial phase-transition to a lower-symmetry state when they are annealed at 1400 °C. This result is consistent with previously reported ternary $\text{Y}_2\text{O}_3\text{-Nd}_2\text{O}_3\text{-ZrO}_2$ phase diagrams calculated at 1400 °C and 1600 °C [60]. These phase diagrams showed that the range of $\text{Nd}_2\text{O}_3\text{-ZrO}_2$ mixtures that stabilized the fluorite phase decreased with decreasing temperature, and help explain how the materials synthesized at 1500 °C were not stable when annealed at 1400 °C.

The energy dispersive spectroscopy (EDS) maps (cf. Figures 5 and 6) showed that Nd inclusions were present in both the $\text{Nd}_x\text{Zr}_{1-x}\text{O}_{2-\delta}$ and $\text{Nd}_x\text{Y}_y\text{Zr}_{1-x-y}\text{O}_{2-\delta}$ materials, and that Zr inclusions were present in the $\text{Nd}_x\text{Zr}_{1-x}\text{O}_{2-\delta}$ materials. It is possible that the Nd and Zr inclusions were observed due to shortcomings in the synthetic process. Given that the materials were made via a high-temperature solid-state reaction using the binary oxides powders as starting materials, it is likely that the reaction kinetics were limited by the rate of solid-state diffusion. If the initial starting powders were not thoroughly mixed to a homogenous state, small heterogeneous regions would be expected as the Nd, Y, and Zr atoms will not be able to diffuse to a homogenous state within a reasonable time period. The SEM and EDS results highlight the difficulty of generating a true $\text{Nd}_x\text{Y}_y\text{Zr}_{1-x-y}\text{O}_{2-\delta}$ solid-solution, and the importance of the synthetic procedure when making these materials.

The fits of the Zr K-edge EXAFS spectra indicated that the σ^2 parameter of Zr–Nd scattering paths in the $\text{Nd}_{0.25}\text{Zr}_{0.75}\text{O}_{1.88}$ increased upon annealing at 1400 °C. These results indicate that the disorder between the metal-centred polyhedra increased upon annealing, and suggest that Nd and Zr became further segregated upon annealing. Segregation of Zr and Nd upon annealing was also observed by EDS, and both Zr-rich and Nd-rich inclusions were observed in the annealed $\text{Nd}_{0.25}\text{Zr}_{0.75}\text{O}_{1.88}$ material. The powder XRD results showed that monoclinic and tetragonal zirconia phases were formed when $\text{Nd}_x\text{Zr}_{1-x}\text{O}_{2-\delta}$ was annealed at 1400 °C, and these phases likely account for the Zr-rich inclusions. No Nd-rich phase was observed by powder XRD in any of the materials. This likely indicates that Nd-rich phase(s) were either present at concentrations below the XRD detection limit or adopted a low-symmetry crystal structure. The former seems more likely given that powder

XRD is relatively insensitive to very low concentration phases [61]. The formation of Nd and Zr rich-phases provides an explanation for the formation of monoclinic and tetragonal ZrO_2 that was observed upon annealing. Nd and Zr became further segregated upon annealing, and Zr-rich inclusions were formed. These inclusions contained an insufficient amount of Nd to allow for stabilization of the fluorite structure, resulting in the formation of lower-symmetry tetragonal and monoclinic phases. No tetragonal or monoclinic zirconia phases were observed in the $Nd_xY_yZr_{1-x-y}O_{2-\delta}$ materials and Zr inclusions were not observed when these materials were annealed at temperatures up and including to 1400 °C. This was likely observed because Y stabilized the cubic structure, which prevented Zr migration in these materials.

5. Conclusions

The thermal stability of the long-range and local structures in the $Nd_xY_yZr_{1-x-y}O_{2-\delta}$ series was characterized in order to assess the applicability of these materials as IMFs. The results showed that both monoclinic and tetragonal zirconia phases were formed when the $Nd_xZr_{1-x}O_{2-\delta}$ materials were annealed at 1400 °C. Therefore, the ternary materials are not suitable candidates for IMF applications. The addition of a small amount of Y ($y \geq 0.05$) stabilized these materials at temperatures up to and including 1400 °C, and the quaternary materials should still be considered as IMF materials. The EXAFS results showed that Y and Zr occupy different coordination environments, and these differences in coordination are not visible by XRD. The SEM and EDS images indicated the presence of Nd inclusions randomly distributed in the materials studied here, and Nd inclusions were observed regardless of composition and annealing temperature. Based on these results, it appears that the synthetic method used to produce these materials must be improved if these materials are to be used in IMF applications. This study also indicated the importance of understanding changes in the structure on both long-range and local scales and showed the utility of using XAS techniques in studying cubic stabilized zirconia materials for IMF applications.

6. Acknowledgements

The Natural Sciences and Engineering Research Council (NSERC) of Canada supported this work through a discovery grant awarded to APG. JRH would also like to thank NSERC for financial support through the Canada Graduate Scholarship program and the University of Saskatchewan. The Canadian Foundation for

Innovation (CFI) is thanked for providing funds to purchase the PANalytical Empyrean powder X-ray diffractometer used in this work. The authors extend their thanks to Dr. Zou Finfrock and Dr. Robert Gordon for their help in carrying out XANES measurements at 20BM (PNC/XSD-CAT, APS), and Ms. Aimee MacLennan and Dr. Youngfeng Hu for help in carrying out the XANES measurements on the SXRMB beamline (06B1-1, CLS). In addition, Mr. M. R. Ruffadin and Ms. E. Aluri (Department of Chemistry, University of Saskatchewan) are thanked for helping with the collection of the XANES spectra presented in this study. The authors would like to thank Dr. R. Ham-Su and Dr. L. Dickson of the Canadian Nuclear Laboratories Limited (CNL) for support of this work. Mr. J. Mouris and Mr. C. Mayhew (CNL) are thanked for their help in the sample preparation for SEM and for collecting the SEM images and EDS measurements. Access to Sector 20 was obtained through the CLS-APS Partnership Agreement. Use of the Advanced Photon Source, an Office of Science User Facility operated for the U.S. Department of Energy (DOE) Office of Science by Argonne National Laboratory, was supported by the U.S. DOE under Contract No. DE-AC02-06CH11357. The CLS is supported by NSERC, the National Research Council of Canada, the Canadian Institutes of Health Research, the Province of Saskatchewan, Western Economic Diversification Canada, and the University of Saskatchewan.

References

- [1] G. Ledergerber, C. Degueldre, P. Heimgartner, M.A. Pouchon, U. Kasemeyer, *Prog. Nucl. Energy* 38 (2001) 301.
- [2] C. Degueldre, J.M. Paratte, *J. Nucl. Mater.* 274 (1999) 1.
- [3] C. Lombardi, A. Mazzola, *Ann. Nucl. Energy* 23 (1996) 1117.
- [4] E.M. González-Romero, *Nucl. Eng. Des.* 241 (2011) 3436.
- [5] C. Degueldre, *J. Alloys Compd.* 444-445 (2007) 36.
- [6] L.M. Wang, S.X. Wang, S. Zhu, R.C. Ewing, *J. Nucl. Mater.* 289 (2001) 122.
- [7] L.M. Wang, S.X. Wang, R.C. Ewing, *Philos. Mag. Lett.* 80 (2000) 341.
- [8] E.A. Schneider, M.R. Deinert, S.T. Herring, K.B. Cady, *J. Nucl. Mater.* 361 (2007) 41.
- [9] C. Degueldre, C. Hellwig, *J. Nucl. Mater.* 320 (2003) 96.
- [10] K. Holliday, T. Hartmann, F. Poineau, J. Rory Kennedy, K. Czerwinski, *J. Nucl. Mater.* 393 (2009) 224.
- [11] C. Degueldre, M. Pouchon, M. Döbeli, K. Sickafus, K. Hojou, G. Ledergerber, S. Abolhassani-Dadras, *J. Nucl. Mater.* 289 (2001) 115.
- [12] K. Holliday, T. Hartmann, K. Czerwinski, *J. Nucl. Mater.* 392 (2009) 487.
- [13] N. Kamel, H. Aït-Amar, M. Taouinet, C. Benazzouz, Z. Kamel, H. Fodil-Cherif, S. Telmoune, R. Slimani, A. Zahri, D. Sahel, *Prog. Nucl. Energy* 48 (2006) 70.
- [14] P. Pöml, R.J.M. Konings, J. Somers, T. Wiss, G.J.L.M. de Haas, F.C. Klaassen, in: R.J.M. Konings, T.R. Allen, R.E. Stoller, S. Yamanaka (Eds.), *Compr. Nucl. Mater.* Vol. 3, 1st ed., Elsevier, 2012, pp. 237–256.
- [15] M. Walter, C. Nästren, J. Somers, R. Jardin, M.A. Denecke, B. Brendebach, *J. Solid State Chem.* 180 (2007) 3130.
- [16] R.C. Belin, P.M. Martin, P.J. Valenza, A.C. Scheinost, *Inorg. Chem.* 48 (2009) 5376.
- [17] S.P. Miller, B.I. Dunlap, A.S. Fleischer, *Solid State Ionics* 227 (2012) 66.
- [18] K. Momma, F. Izumi, *J. Appl. Crystallogr.* 41 (2008) 653.
- [19] G.R. Lumpkin, *Elements* 2 (2006) 365.
- [20] M.H. Bocanegra-Bernal, S. Díaz de la Torre, *J. Mater. Sci.* 37 (2002) 4947.
- [21] F. Zhang, P.J. Chupas, S.L.A. Lui, J.C. Hanson, W.A. Caliebe, P.L. Lee, S.-W. Chan, *Chem. Mater.* 19 (2007) 3118.

- [22] N. Shibata, J. Katamura, A. Kuwabara, Y. Ikuhara, T. Sakuma, *Mater. Sci. Eng. A* 312 (2001) 90.
- [23] V.G. Zavodinsky, A.N. Chibisov, *Phys. Solid State* 48 (2006) 363.
- [24] R.C. Garvie, R.H. Hannink, R.T. Pascoe, *Nature* 258 (1975) 703.
- [25] R.H.J. Hannink, P.M. Kelly, B.C. Muddle, *J. Am. Ceram. Soc.* 83 (2000) 461.
- [26] A.S. Nesaraj, *J. Sci. Ind. Res.* 69 (2010) 169.
- [27] J.E. Petitjean, R.M. Kearsey, X. Huang, *Surf. Coatings Technol.* 205 (2010) 1843.
- [28] C.K. Chow, H.F. Khartabil, *Nucl. Eng. Technol.* 40 (2007) 139.
- [29] M.A. Pouchon, C. Degueldre, P. Tissot, *Thermochim. Acta* 323 (1998) 109.
- [30] T. Arima, Y. Tokura, J. Torrance, *Phys. Rev. B* 48 (1993) 17006.
- [31] C. Ronchi, J.P. Ottaviani, C. Degueldre, R. Calabrese, *J. Nucl. Mater.* 320 (2003) 54.
- [32] X. Guo, *Phys. Status Solidi* 177 (2000) 191.
- [33] R. Villarreal, D. Spall, *Selection of Actinide Chemical Analogues for WIPP Tests*, Los Alamos, 1995.
- [34] R.D. Shannon, *Acta Crystallogr., Sect. A Found. Crystallogr.* 32 (1976) 751.
- [35] G.T. Seaborg, *Radiochim. Acta* 61 (1993) 115.
- [36] S. Lemonnier, S. Grandjean, A.-C. Robisson, J.-P. Jolivet, *Dalton Trans.* 39 (2010) 2254.
- [37] PANalytical HighScore Plus Version 3.0.4 (2011) PANalytical BV: Amelo, The Netherlands..
- [38] J. Jaffe, R. Bachorz, M. Gutowski, *Phys. Rev. B* 72 (2005) 144107.
- [39] N. Igawa, Y. Ishii, *J. Am. Ceram. Soc.* 84 (2001) 1169.
- [40] B. Bondars, G. Heidemane, J. Grabis, K. Laschke, H. Boysen, J. Schneider, F. Frey, *J. Mater. Sci.* 30 (1995) 1621.
- [41] S.M. Heald, D.L. Brewster, E.A. Stern, K.H. Kim, F.C. Brown, D.T. Jiang, E.D. Crozier, R.A. Gordon, *J. Synchrotron Rad.* 6 (1999) 347.
- [42] A. Thompson, D. Attwood, E. Gullikson, M. Howells, K.-J. Kim, J. Kirz, J. Kortright, I. Lindau, P. Pianetta, A. Robinson, J. Scofield, J. Underwood, D. Vaughn, G. Williams, H. Winick, *X-Ray Data Booklet*, Lawrence Berkeley National Laboratory, Berkeley, 2009.
- [43] B. Ravel, M. Newville, *J. Synchrotron Rad.* 12 (2005) 537.
- [44] M. Newville, *Fundamentals of XAFS*, 1.7 ed., University of Chicago, Chicago, 2004.
- [45] J. Rehr, R. Albers, *Phys. Rev. B* 41 (1990) 8139.

- [46] P. Li, I.-W. Chen, J.E. Penner-Hahn, *Phys. Rev. B* 48 (1993) 10074.
- [47] Y.F. Hu, I. Coulthard, D. Chevrier, G. Wright, R. Igarashi, A. Sitnikov, *AIP Conf. Proc.* 1234 (2010) 343.
- [48] A. Denton, N. Ashcroft, *Phys. Rev. A* 43 (1991) 3161.
- [49] G. Mountjoy, D.M. Pickup, R. Anderson, G.W. Wallidge, M.A. Holland, R.J. Newport, M.E. Smith, *Phys. Chem. Chem. Phys.* 2 (2000) 2455.
- [50] G. Mountjoy, M.A. Holland, G.W. Wallidge, P. Gunawidjaja, M.E. Smith, D.M. Pickup, R.J. Newport, *J. Phys. Chem. B* 107 (2003) 7557.
- [51] P. VILLELLA, S. Conradson, F. Espinosa-Faller, S. Foltyn, K. Sickafus, J. Valdez, C. Degueldre, *Phys. Rev. B* 64 (2001) 104101.
- [52] C.R.A. Catlow, A. V Chadwick, G.N. Greaves, L.M. Moroney, *J. Am. Ceram. Soc.* 69 (1986) 272.
- [53] A. Gómez, R. Villanueva, D. Vie, S. Murcia-Mascaros, E. Martínez, A. Beltrán, F. Sapiña, M. Vicent, E. Sánchez, *J. Solid State Chem.* 197 (2013) 120.
- [54] P. Li, I. Chen, J.E. Penner-Hahn, *Phys. Rev. B* 48 (1993) 10082.
- [55] P.E.R. Blanchard, S. Liu, B.J. Kennedy, C.D. Ling, Z. Zhang, M. Avdeev, B.C.C. Cowie, L. Thomsen, L.-Y. Jang, *Dalton Trans.* 42 (2013) 14875.
- [56] P.E.R. Blanchard, R. Clements, B.J. Kennedy, C.D. Ling, E. Reynolds, M. Avdeev, A.P.J. Stampfl, Z. Zhang, L.-Y. Jang, *Inorg. Chem.* 51 (2012) 13237.
- [57] C. Artini, M. Pani, A. Lausi, R. Masini, G.A. Costa, *Inorg. Chem.* 53 (2014) 10140.
- [58] M. Zinkevich, *Prog. Mater. Sci.* 52 (2007) 597.
- [59] Z. Wu, M. Benfatto, C. Natoli, *Phys. Rev. B* 57 (1998) 10336.
- [60] O. Fabrichnaya, G. Savinykh, G. Schreiber, H.J. Seifert, *J. Phase Equilibria Diffus.* 32 (2011) 284.
- [61] B.A. Sarsfield, M. Davidovich, S. Desikan, M. Fakes, S. Futernik, J.L. Hilden, J.S. Tan, S. Yin, G. Young, B. Vakkalagadda, K. Volk, *Adv. X-Ray Sci.* 49 (2006) 322.

Tables

Table 1: Summary of powder XRD Rietveld Refinement Results

Nd_{0.25}Zr_{0.75}O_{1.88}		
	As synthesized	Annealed 1400 °C
R _{wp} ^a	7.14	9.00
Unit Cell ^b	5.2089(7)	5.2060(1)
Wt. Fraction	100% Cubic	84.5% Cubic 11.3% Monoclinic 4.2% Tetragonal

Nd_{0.20}Y_{0.05}Zr_{0.75}O_{1.88}		
	As synthesized	Annealed 1400 °C
R _{wp} ^a	7.05	12.29
Unit Cell ^b	5.1977(6)	5.1932(1)
Wt. Fraction	100% Cubic	100% Cubic

Nd_{0.05}Y_{0.20}Zr_{0.75}O_{1.88}		
	As synthesized	Annealed 1400 °C
R _{wp} ^a	8.66	12.74
Unit Cell ^b	5.1658(6)	5.1639(1)
Wt. Fraction	100% Cubic	100% Cubic

Y_{0.25}Zr_{0.75}O_{1.88}		
	As synthesized	Annealed 1400 °C
R _{wp} ^a	7.41	9.38
Unit Cell ^b	5.1555(7)	5.1494(1)
Wt. Fraction	98.3% Cubic 1.7% Monoclinic	100% Cubic

^aR_{wp} = $\sum w_i (y_{io} - y_{ic})^2 / \sum w_i y_{io}$; w_i = ith comp. wt. fraction; y_{ic} = calculated intensity; y_{io} = diffraction pattern intensity.

^bCubic unit cell parameter

Table 2: Zr K-edge EXAFS Results

Nd_{0.25}Zr_{0.75}O_{1.88}						
	As-synthesized			Annealed 1400 °C		
	S _o ² = 0.8(1), ΔE = -4(1) eV R _{fit} = 0.030			S _o ² = 0.9(1) ΔE = 4(1) eV R _{fit} = 0.028		
	CN	R (Å)	σ ²	CN	R (Å)	σ ²
Zr-O	7	2.15(1)	0.007(1)	7	2.16(1)	0.007(1)
Zr-Zr	9	3.55(1)	0.010(1)	9	3.54(1)	0.011(1)
Zr-Nd	3	3.72(4)	0.010(5)	3	3.8(1)	0.02(2)
Zr-O2	22	4.38(5)	0.04(2)	22	4.43(5)	0.04(2)

Nd_{0.20}Y_{0.05}Zr_{0.75}O_{1.88}						
	As-synthesized			Annealed 1400 °C		
	S _o ² = 0.87(9) ΔE = -4(1) eV R _{fit} = 0.028			S _o ² = 0.93(9) ΔE = -2(1) eV R _{fit} = 0.020		
	CN	R (Å)	σ ²	CN	R (Å)	σ ²
Zr-O	7	2.16(1)	0.006(1)	7	2.15(1)	0.008(2)
Zr-Zr/Y	9.6	3.56(2)	0.011(2)	9.6	3.56(1)	0.012(2)
Zr-Nd	2.4	3.8(1)	0.013(9)	2.4	3.71(3)	0.009(4)
Zr-O2	22	4.40(6)	0.04(2)	22	4.34(7)	0.04(2)

Table 3: Y K-edge EXAFS Fitting Results

Y_{0.25}Zr_{0.75}O_{1.88}									
	As-synthesized S _o ² = 0.9(1) ΔE = -3(1) eV R _{fit} = 0.033			Annealed 900 °C S _o ² = 1.2(2) ΔE = -6(1) eV R _{fit} = 0.011			Annealed 1400 °C S _o ² = 0.9(1) ΔE = -3(1) eV R _{fit} = 0.033		
	CN	R (Å)	σ ²	CN	R (Å)	σ ²	CN	R (Å)	σ ²
Y-O	8	2.32(1)	0.009(2)	8	2.32(1)	0.012(2)	8	2.32(1)	0.008(2)
Y-Zr/Y	12	3.626(8)	0.008(1)	12	3.616(9)	0.009(1)	12	3.626(8)	0.007(1)
Y-O2	22	4.39(9)	0.03(2)	22	4.29(7)	0.027(8)	22	4.36(6)	0.02(1)
Nd_{0.20}Y_{0.05}Zr_{0.75}O_{1.88}									
	As-synthesized S _o ² = 1.1(1) ΔE = -3(8) eV R _{fit} = 0.022			Annealed 900 °C S _o ² = 0.77(8) ΔE = -4(1) eV R _{fit} = 0.018			Annealed 1400 °C S _o ² = 0.86(9) ΔE = -4(1) eV R _{fit} = 0.01		
	CN	R (Å)	σ ²	CN	R (Å)	σ ²	CN	R (Å)	σ ²
Y-O	8	2.32(1)	0.009(2)	8	2.33(1)	0.009(2)	8	2.33(1)	0.009(1)
Y-Zr/Y	9.6	3.639(8)	0.008(1)	9.6	3.66(1)	0.008(2)	9.6	3.632(8)	0.0092(7)
Y-Nd	2.4	3.52(9)	0.02(2)	2.4	3.41(3)	0.005(2)	2.4	3.4(1)	0.03(2)
Y-O2	22	4.40(6)	0.03(1)	22	4.1(2)	0.1(1)	22	4.42(6)	0.03(1)

Figure Captions

Figure 1 The fluorite structure of cubic zirconia is shown. Zr, Y, and Nd are randomly distributed in one 8-fold coordination site (blue spheres), and the O (red-spheres) adopts a 4-fold coordination environment in this structure. All atoms occupy special positions [17,18].

Figure 2 The powder X-ray diffraction patterns of the as-synthesized and annealed materials from (a) $\text{Nd}_{0.25}\text{Zr}_{0.75}\text{O}_{1.88}$ and (b) $\text{Nd}_{0.10}\text{Y}_{0.10}\text{Zr}_{0.80}\text{O}_{1.90}$ are plotted along with patterns generated by Rietveld refinement of the data. (Annealed materials are labelled as “An”.) The intensities of the (220) reflections found at $\sim 58^\circ$ and the (311) reflections found at $\sim 69.6^\circ$ were generally underfit by the simulated pattern, which may indicate a deviation from the ideal stoichiometry in these materials. The XRD patterns from $\text{Nd}_{0.25}\text{Zr}_{0.75}\text{O}_{1.88}$ indicate that small amounts of monoclinic and tetragonal ZrO_2 was formed when the material was annealed at 1400°C , as shown by the peaks marked with asterisks. No changes in the diffraction patterns were observed when the $\text{Nd}_{0.10}\text{Y}_{0.10}\text{Zr}_{0.80}\text{O}_{1.90}$ material was annealed.

Figure 3 The diffraction patterns from as-synthesized $\text{Nd}_{0.25}\text{Zr}_{0.75}\text{O}_{1.88}$ and $\text{Nd}_{0.25}\text{Zr}_{0.75}\text{O}_{1.88}$ materials annealed at 1400°C are presented. The diffraction patterns show that small amounts of tetragonal and monoclinic ZrO_2 are formed when $\text{Nd}_{0.25}\text{Zr}_{0.75}\text{O}_{1.88}$ is annealed at 1400°C .

Figure 4 Secondary electron micrographs from (a) as-synthesized $\text{Nd}_{0.25}\text{Zr}_{0.75}\text{O}_{1.88}$ and (c) $\text{Nd}_{0.25}\text{Zr}_{0.75}\text{O}_{1.88}$ annealed at 1400°C are presented. The backscattering electron micrographs from (b) as-synthesized $\text{Nd}_{0.25}\text{Zr}_{0.75}\text{O}_{1.88}$ and (d) $\text{Nd}_{0.25}\text{Zr}_{0.75}\text{O}_{1.88}$ annealed at 1400°C are also presented. The secondary electron images show that there were no significant changes in the pellet surface when the materials were annealed. Bright spots in the backscattered electron images indicate that Nd-rich inclusions were present in these materials. A $50\ \mu\text{m}$ scale bar is included in (b) and the scale for all the images is the same.

Figure 5 Nd EDS maps from (a) as-synthesized $\text{Nd}_{0.25}\text{Zr}_{0.75}\text{O}_{1.88}$, (b) as-synthesized $\text{Nd}_{0.10}\text{Y}_{0.10}\text{Zr}_{0.80}\text{O}_{1.90}$, (c) $\text{Nd}_{0.25}\text{Zr}_{0.75}\text{O}_{1.88}$ annealed at 1400°C , and (d) $\text{Nd}_{0.10}\text{Y}_{0.10}\text{Zr}_{0.80}\text{O}_{1.90}$ annealed at 1400°C are presented. The maps

were collected in the same region and at the same magnification as the micrographs presented in Figure 4. These maps confirm that Nd was not homogeneously distributed in these materials. A 100 μm scale bar is included in (a), and the scale for all the images is the same.

Figure 6 Zr EDS maps from (a) as-synthesized $\text{Nd}_{0.25}\text{Zr}_{0.75}\text{O}_{1.88}$, (b) as-synthesized $\text{Nd}_{0.10}\text{Y}_{0.10}\text{Zr}_{0.80}\text{O}_{1.90}$, (c) $\text{Nd}_{0.25}\text{Zr}_{0.75}\text{O}_{1.88}$ annealed at 1400 $^{\circ}\text{C}$, and (d) $\text{Nd}_{0.10}\text{Y}_{0.10}\text{Zr}_{0.80}\text{O}_{1.90}$ annealed at 1400 $^{\circ}\text{C}$ are presented. The maps were collected in the same region and at the same magnification as the micrographs presented in Figure 4. The maps show that Zr was not homogeneously distributed in the $\text{Nd}_{0.25}\text{Zr}_{0.75}\text{O}_{1.88}$ materials. A 100 μm scale bar is included in (a), and the scale for all the images is the same.

Figure 7 (a) Zr K-edge XANES spectra from the as-synthesized $\text{Nd}_x\text{Y}_x\text{Zr}_{1-x-y}\text{O}_{2-\delta}$ materials are presented. Three features, A, B, and B' were observed and correspond to quadrupolar (A) and dipolar (B, B') transitions. The Zr K-edge spectra did not change with changes in composition. (b) The Zr K-edge XANES spectra from the as-synthesized and annealed $\text{Nd}_{0.25}\text{Zr}_{0.75}\text{O}_{1.88}$ and $\text{Nd}_{0.20}\text{Y}_{0.05}\text{Zr}_{0.75}\text{O}_{1.88}$ materials are compared. A slight increase in intensity was observed at around 18025 eV when the $\text{Nd}_{0.25}\text{Zr}_{0.75}\text{O}_{1.88}$ material was annealed at 1400 $^{\circ}\text{C}$ and peak B' shifted to slightly lower energy. *Inset*: A close-up view of the change observed in the main-edge region of the spectra from as-synthesized $\text{Nd}_{0.25}\text{Zr}_{0.75}\text{O}_{1.88}$ and $\text{Nd}_{0.25}\text{Zr}_{0.75}\text{O}_{1.88}$ annealed at 1400 $^{\circ}\text{C}$. (c) The Zr K-edge XANES spectra from $\text{Nd}_{0.25}\text{Zr}_{0.75}\text{O}_{1.88}$, tetragonal ZrO_2 ($\text{Y}_{0.09}\text{Zr}_{0.81}\text{O}_{1.96}$), and monoclinic ZrO_2 are compared. The separation of features B and B' decreased with decreasing symmetry of the unit cell.

Figure 8 (a) The magnitudes of the Fourier-transformed Zr K-edge EXAFS spectra from the as-synthesized materials are compared. Two features were observed in these spectra, labelled as C and D. Feature C was due to Zr–O single scattering paths and feature D was due to Zr–Zr/Y/Nd single scattering paths. Feature C was independent of composition while feature D increased with decreasing Nd content. (b) The real part of the Fourier transformed Zr K-edge EXAFS spectrum from $\text{Nd}_{0.25}\text{Zr}_{0.75}\text{O}_{1.88}$ along with the real portions of the contributions from the Zr–Zr (CN=9) and Zr –Nd (CN=3) scattering paths are shown. The sum of these scattering path contributions is compared to the contribution from a Zr–Zr path with CN = 12. The oscillations in the summed

scattering path are reduced compared to the Zr–Zr scattering path with CN = 12 and better match the data. (c) The magnitudes of the scattering path contributions from the Zr–Zr and Zr–Nd single scattering paths (i.e., Feature D) are compared with the Zr K-edge EXAFS spectrum from $\text{Nd}_{0.25}\text{Zr}_{0.75}\text{O}_{1.88}$.

Figure 9 (a) The magnitudes of the Fourier-transformed Zr K-edge EXAFS spectra from the as-synthesized and annealed $\text{Nd}_{0.25}\text{Zr}_{0.75}\text{O}_{1.88}$ materials are compared. Feature C was relatively independent of annealing temperature while there was a decrease in the intensity of peak D when $\text{Nd}_{0.25}\text{Zr}_{0.75}\text{O}_{1.88}$ was annealed at 1400 °C. The EXAFS spectrum from the as-synthesized $\text{Nd}_{0.25}\text{Zr}_{0.75}\text{O}_{1.88}$ is compared with its fit in (b) k-space and (c) real space.

Figure 10 The Zr L_3 -edge XANES spectra from the as-synthesized materials are plotted along with the spectrum from monoclinic ZrO_2 . Features E and F arise from transitions to e_g and t_{2g}^* states, respectively. Feature F decreased as the Nd content decreased.

Figure 11 The magnitudes of the Fourier transformed Y K-edge EXAFS spectra from the as-synthesized materials are presented. Feature G arises due to Y–O single-scattering paths and feature H is attributed to Y–Y/Zr/Nd single scattering paths. The intensity of both features increased with decreasing Nd content.

Figure 12 (a) The magnitudes of the Fourier transformed Y K-edge EXAFS spectra from the as-synthesized and annealed $\text{Nd}_{0.20}\text{Y}_{0.05}\text{Zr}_{0.75}\text{O}_{1.88}$ materials are plotted. Feature G changes slightly with annealing temperature while feature H was independent of annealing temperature. The EXAFS spectrum from the as-synthesized $\text{Nd}_{0.20}\text{Y}_{0.05}\text{Zr}_{0.75}\text{O}_{1.88}$ is compared with its fit in (b) k-space and (c) real space.

Figure 13 The Nd L_3 -edge XANES spectra from as-synthesized and annealed $\text{Nd}_x\text{Y}_y\text{Zr}_{1-x-y}\text{O}_{2-\delta}$ materials are presented. The strong white-line feature at 6014 eV is due to Nd $2p \rightarrow \text{Nd } 5d$ transitions. No changes in the spectra were observed between the as-synthesized and annealed materials.

Figures

Figure 1

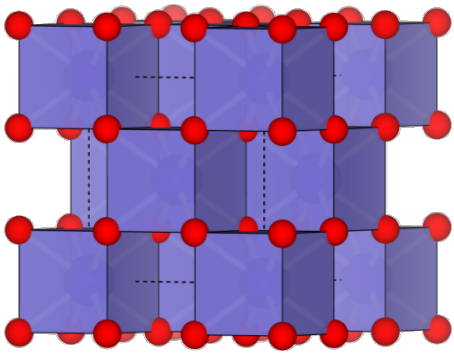


Figure 2

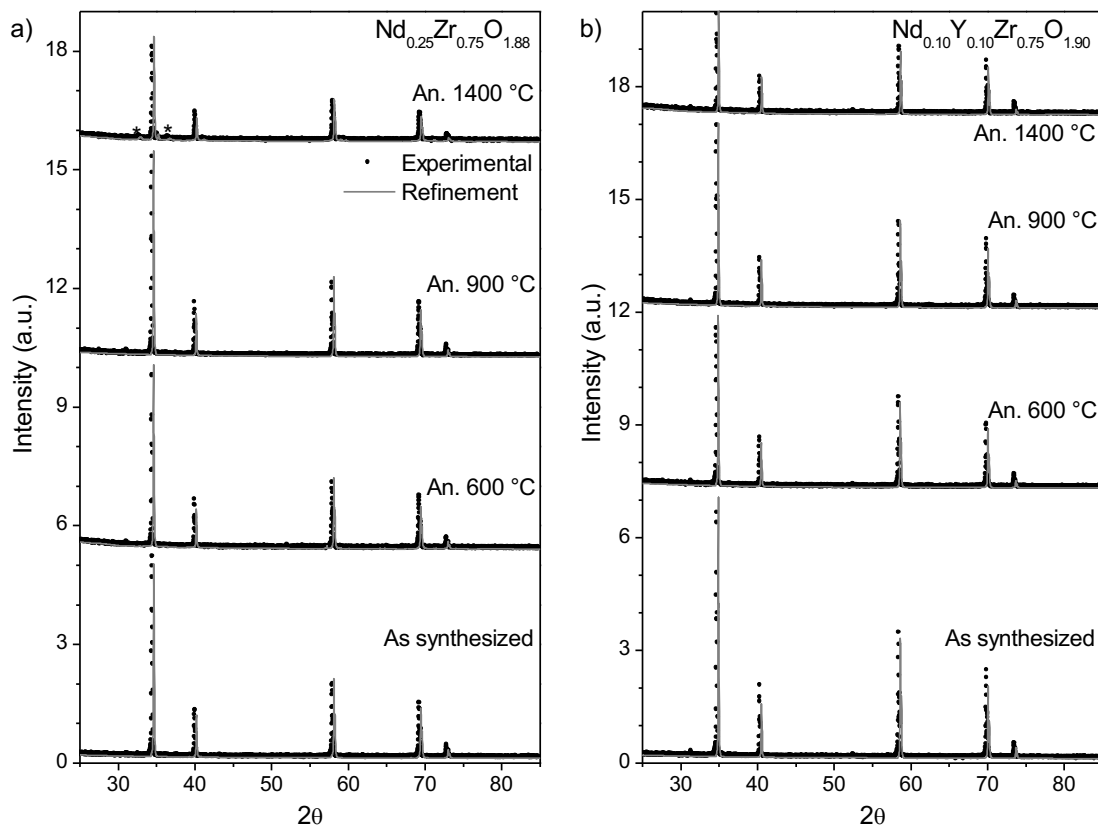


Figure 3

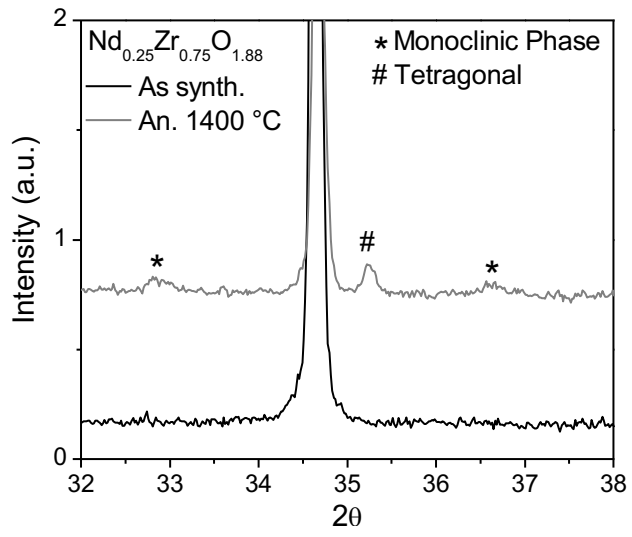


Figure 4

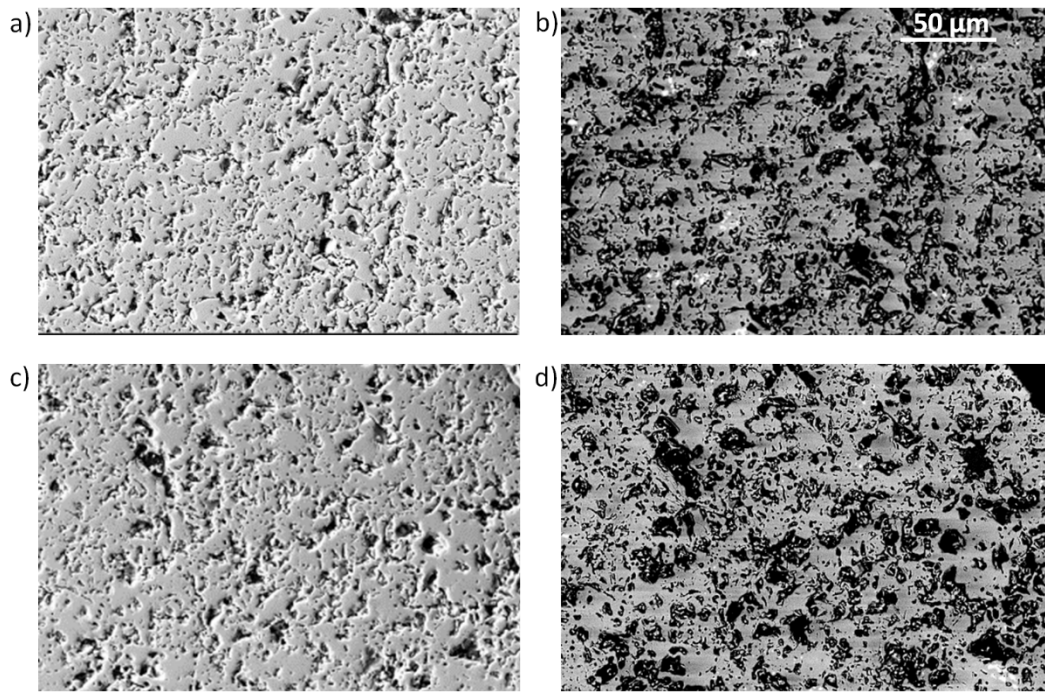


Figure 5

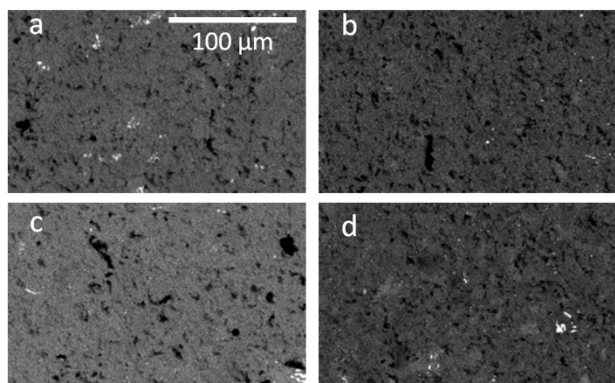


Figure 6

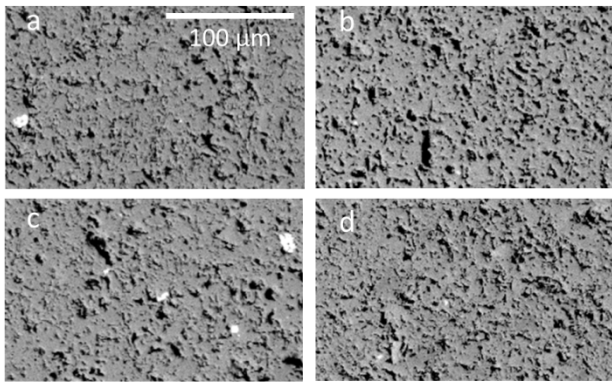


Figure 7

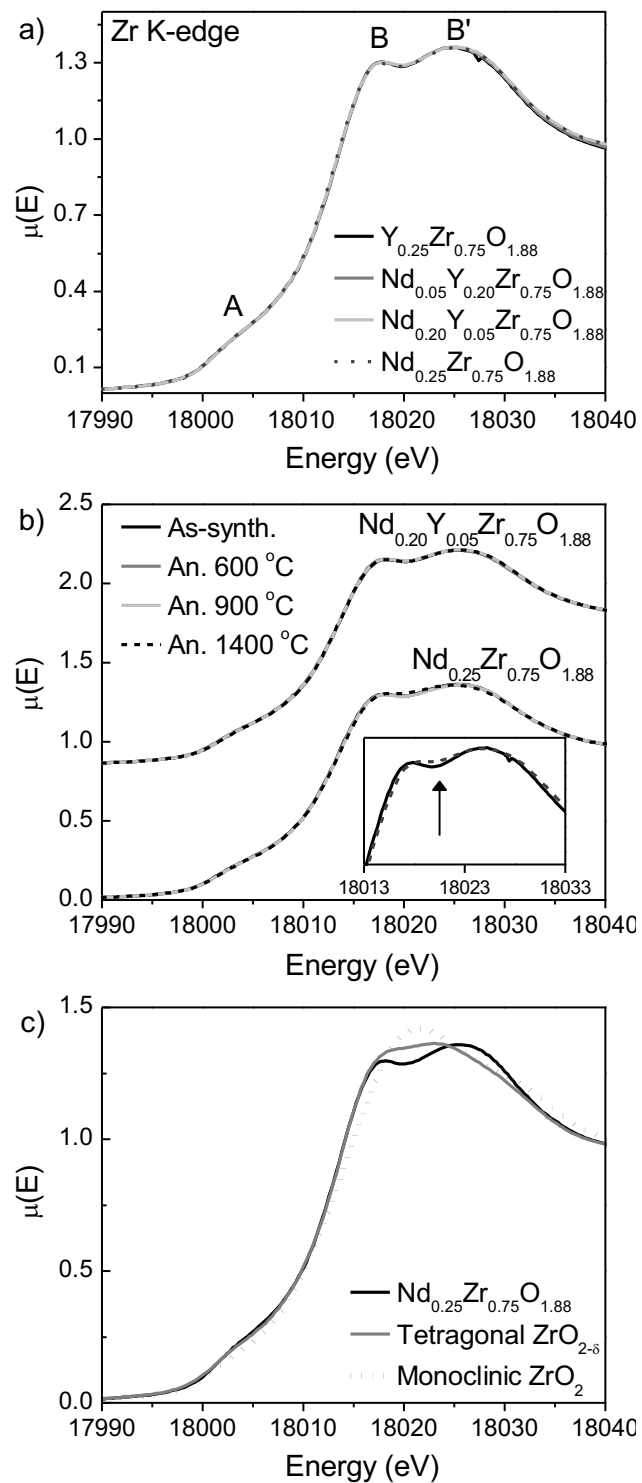


Figure 8

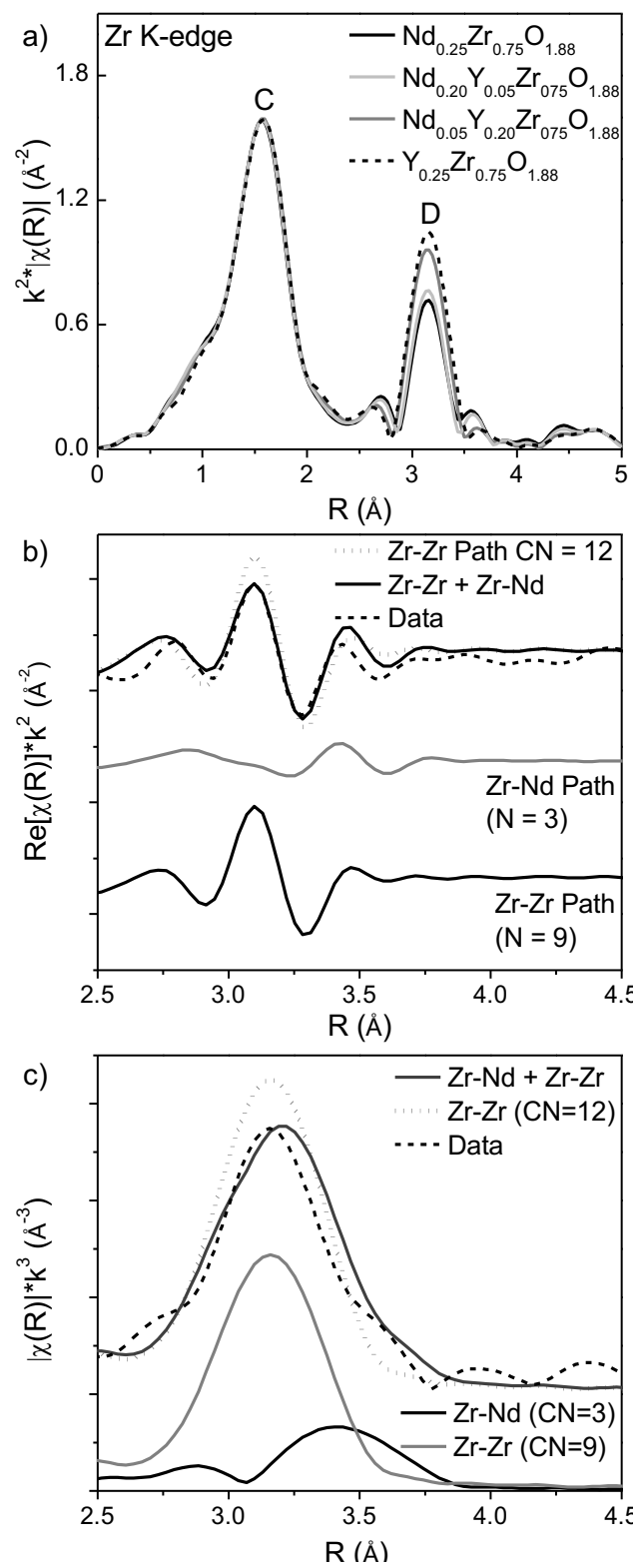


Figure 9

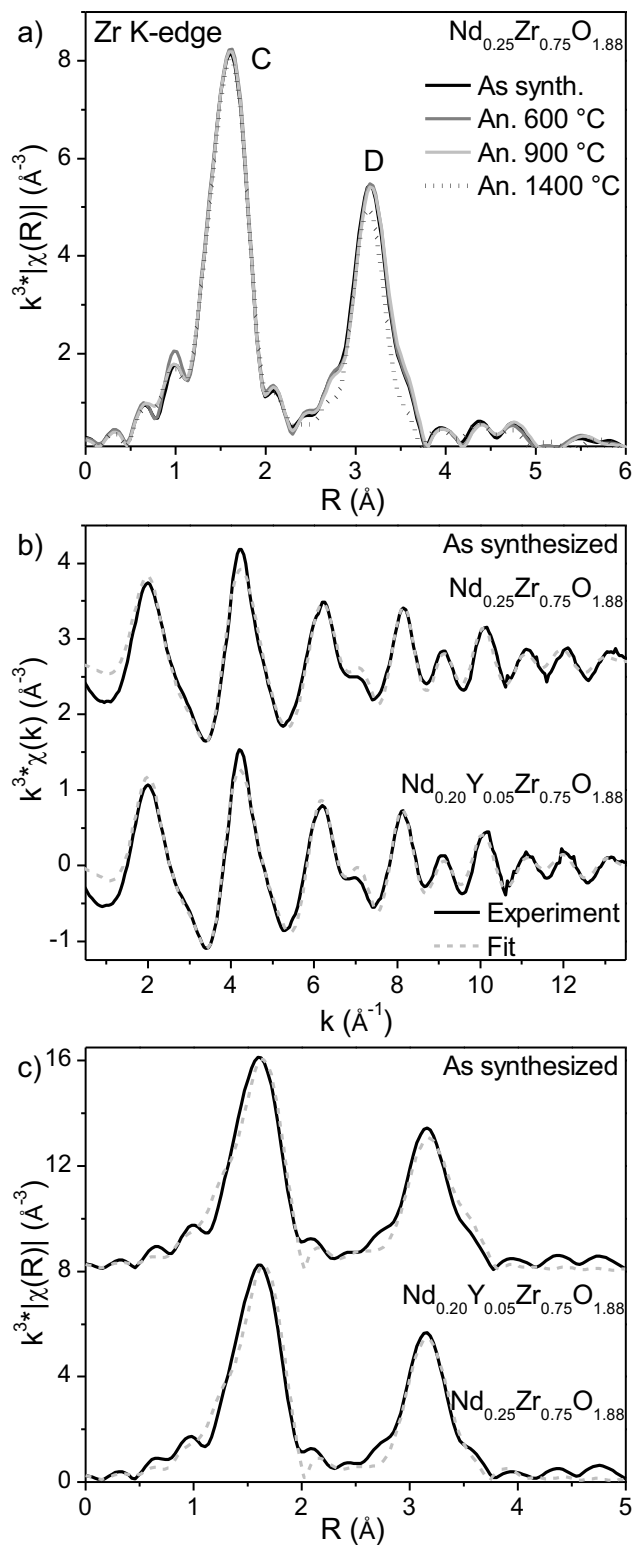


Figure 10

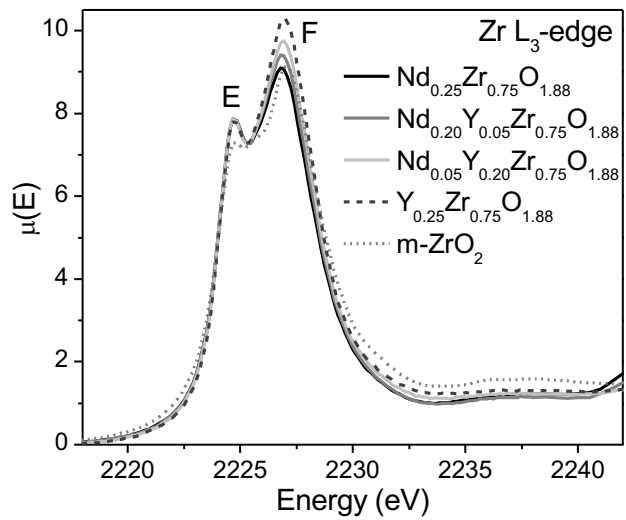


Figure 11

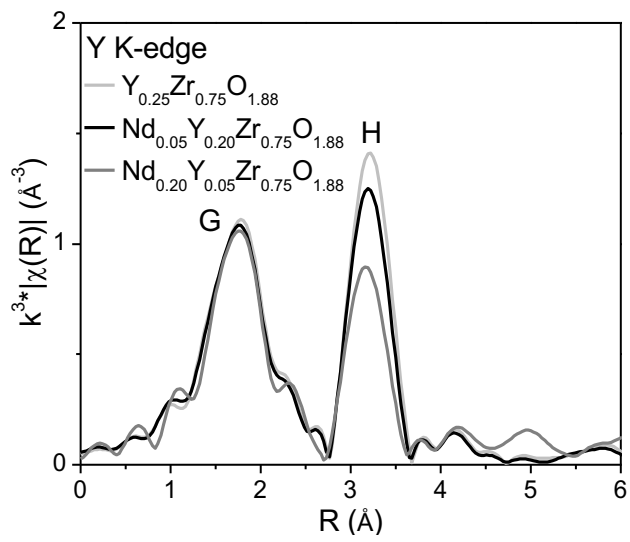


Figure 12

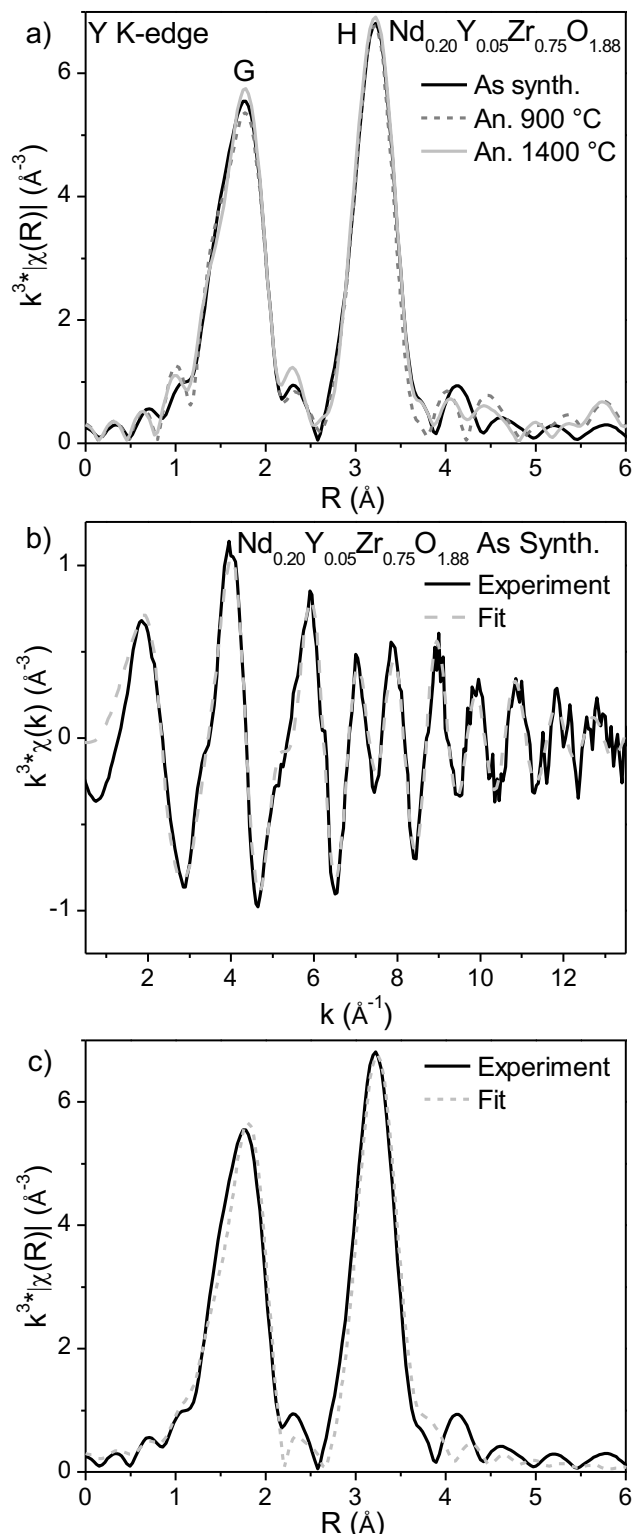


Figure 13

